Applied Surface Science 579 (2022) 152210

Contents lists available at ScienceDirect

Applied Surface Science

journal homepage: www.elsevier.com/locate/apsusc

Full Length Article

Mechanistic explanation for differences between catalytic activities of dissolved and aerogel immobilized Cu(II) cyclen

Attila Forgács [a], Zoltán Balogh [a,b], Melinda Andrási [a], Adél Len [b], Zoltán Dudás [b], Nóra V. May [c], Petra Herman [a], Laura Juhász [d], István Fábián [a], Norbert Lihi [a,*], József Kalmár [a,*]

[a] Department of Inorganic and Analytical Chemistry, MTA-DE Redox and Homogeneous Catalytic Reaction Mechanisms Research Group, University of Debrecen, Egyetem tér 1, Debrecen H-4032, Hungary
[b] Neutron Spectroscopy Department, Centre for Energy Research, Konkoly-Thege Miklós út 29-33, Budapest H-1121, Hungary
[c] Centre for Structural Science, Research Centre for Natural Sciences, Magyar tudósok körútja 2, Budapest H-1117, Hungary
[d] Department of Solid State Physics, University of Debrecen, Egyetem tér 1, Debrecen H-4032, Hungary

ARTICLE INFO

Keywords:
Aerogel
Cu(II)-cyclen
Reaction kinetics
Reaction mechanism

ABSTRACT

The copper(II) complex of 1,4,7,10-tetraazacyclododecane [Cu(II)-cyclen] was covalently immobilized in mesoporous silica aerogel. This immobilization significantly alters the catalytic activity of Cu(II)-cyclen when referenced to the dissolved complex in the oxidation of phenol by H_2O_2 in aqueous solution. In order to understand this phenomenon, the functionalized aerogel was characterized by scanning electron microscopy (SEM), N_2 porosimetry, small angle neutron scattering (SANS), infrared spectroscopy (IR) and electron paramagnetic resonance spectroscopy (EPR). Aerogel morphology is typical of mesoporous silica aerogels, and the coordination mode of Cu(II) in the immobilized complex is well-related but not identical to solution phase Cu(II)-cyclen. The mechanisms of the catalytic reactions involving dissolved and immobilized Cu(II)-cyclen were explored by fine kinetic experiments using capillary electrophoresis (CE) and on-line UV–vis spectrophotometry. Hydroquinone, pyrocatechol and the related benzoquinones were identified as the main intermediates in both reaction systems. A detailed kinetic model is postulated based on global data fitting, which clearly highlights the mechanistic differences in the two systems. Interestingly, the activation of the catalyst by H_2O_2 is more effective in the case of the aerogel, but the total conversion of phenol is slower due to hindered mass transport compared to using dissolved Cu(II)-cyclen.

1. Introduction

The accumulation of phenol and its various derivatives in wastewater is a global environmental problem. In higher concentrations, they are toxic to most organisms [1]. Chlorinated phenolic derivatives exhibit carcinogenic feature at low concentrations, therefore, the accumulated phenols must be eliminated before the chlorination of the water. Its removal is still difficult, since phenol is not a biodegradable organic compound, and its physical removal requires post-treatment [2–5].

There are several methods to eliminate phenolic compounds from wastewater such as distillation, adsorption, extraction, membrane processes, ozonization and advanced oxidation processes (AOPs) [6–12]. Oxidation with hydrogen peroxide in an aqueous medium in the presence of a catalyst is considered to be an efficient and green process [13–15]. Copper-containing catalysts have successfully been used for oxidizing phenol with H_2O_2 [16–18]. Heterogeneous catalysis is preferred, because the catalyst can be physically separated and recycled. Therefore, the immobilization of efficient catalysts in chemically inert porous supports with large apparent surface area is often sought. An important aspect of utilizing porous catalyst supports is that the reactions take place in confinement inside the pores. Such confinement of the reactants can alter the frequency of the reactive collisions, which can affect the kinetics of the overall catalytic reactions. This could lead to the alteration of the specific activity or the selectivity of the immobilized catalyst compared to the dissolved counterpart used in a homogeneous system. In connection with such phenomena, Derouane et. al. proposed and later extended the theory of “confinement / nest effect”, first for the shape selectivity of zeolites [19,20].

Inorganic oxide (silica, alumina, titania, zirconia, etc.) aerogels are ideal catalyst supports owing to their open mesoporous structures and

* Corresponding authors.
E-mail addresses: lihi.norbert@science.unideb.hu (N. Lihi), kalmar.jozsef@science.unideb.hu (J. Kalmár).

https://doi.org/10.1016/j.apsusc.2021.152210
Received 5 October 2021; Received in revised form 10 December 2021; Accepted 12 December 2021
Available online 16 December 2021

high apparent surface area. Functionalized aerogels have already been successfully applied, e.g. in the dehydrogenation of ammonia, in Fischer-Tropsch processes, in methanol conversion and in the oxidation of carbon monoxide [21–24]. Recently, the cyclen (1,4,7,10-tetraazacyclododecane) and cyclam complexes of Cu(II) were reported to be immobilized in silica aerogel and used for the catalytic oxidation of phenol by H_2O_2 in aqueous solution. Interestingly, the immobilized catalysts displayed distinct specific activities than their dissolved counterparts under otherwise identical conditions. All experimental details including kinetic experiments highlighting the differences between the catalytic activities are given in the referenced publication [25]. However, the detailed mechanistic explanation for the alteration of the catalytic activity of the immobilized complexes has not yet been given.

In this paper, we report the in-depth characterization of the Cu(II) complex of 1,4,7,10-tetraazacyclododecane (denoted as Cu(II)-cyclen through this paper) immobilized on mesoporous silica aerogel support, and the detailed mechanistic investigation of the catalytic oxidation of aqueous phenol by H_2O_2. The catalytic features of dissolved Cu(II)-cyclen (homogeneous catalysis) and that of the Cu(II)-cyclen functionalized aerogel (heterogeneous catalysis) are contrasted to each other. Detailed kinetic models are postulated in the homogeneous and the heterogeneous systems in order to give a mechanistic explanation for the alteration of the specific catalytic activity of Cu(II)-cyclen when immobilized in silica aerogel.

2. Experimental section

2.1. Materials

Tetramethyl orthosilicate (TMOS), 1,4,7,10-tetraazacyclododecane (cyclen), (3-glycidoxy-propyl)-trimethoxysilane (GPTMS), phenol and copper(II) nitrate were purchased from Sigma-Aldrich. Methanol and acetone were purchased from Molar Chemicals Ltd. (Budapest, Hungary). Ammonium carbonate and nitric acid (65%) were purchased from Merck, while 30% hydrogen peroxide and phenol were from VWR. The aqueous solutions were prepared with doubly-deionized and ultrafiltered water (ELGA PureLab classic system). Argon gas cylinders (99.996%) and carbon dioxide cylinders (Biogon-C, 99.5%) equipped with a dip tube were purchased from Linde Gáz Magyarország Zrt. (Debrecen, Hungary).

2.2. Synthesis of functionalized silica aerogels

Copper(II)-cyclen functionalized silica aerogels were prepared by a base catalyzed sol–gel synthesis method published in the literature [25,26]. Because the cyclen moiety easily reacts with the carbon dioxide content of the air, the synthesis was carried out under inert atmosphere. A two-necked flask was flushed with Ar, and 802 mg (4.65 mmol) cyclen was dissolved in the mixture of 32 ml (1.78 mol) water and 63.5 ml (1.09 mol) of ethanol. To this solution 4 ml GPTMS (18.1 mmol) was added, and the mixture was stirred for 30 min at room temperature. The functionalized silica-precursor forms in the reaction between cyclen and GPTMS as illustrated in Scheme 1. In the subsequent step, 1.12 g Cu $(NO_3)_2{\cdot}3H_2O$ (4.63 mmol) dissolved in 20 ml (1.11 mmol) of water was added to the solution. Rapid complex formation was accompanied by change in color from colorless to dark blue. The silica gel was prepared by adding 15.2 ml (102 mmol) TMOS to the system, followed by the addition of 382 mg (3.97 mmol) of ammonium carbonate as a catalyst in 4.0 ml (222 mmol) water. The mixture was poured immediately into a plastic mold. Gelation occurred within a few minutes. The alcogel was kept in the sealed mold for 5 days. The aged gels were placed into methanol for 24 h. After that, multiple step solvent exchange was carried out as follows. Methanol was replaced to a mixture of methanol-acetone 2:1, methanol-acetone 1:1, and finally to pure acetone. Before the supercritical drying, the gel was soaked in freshly distilled acetone for three days to remove residual water. Drying was performed in a pumpless drying system using supercritical CO_2 based on the same protocol as published earlier [26,27].

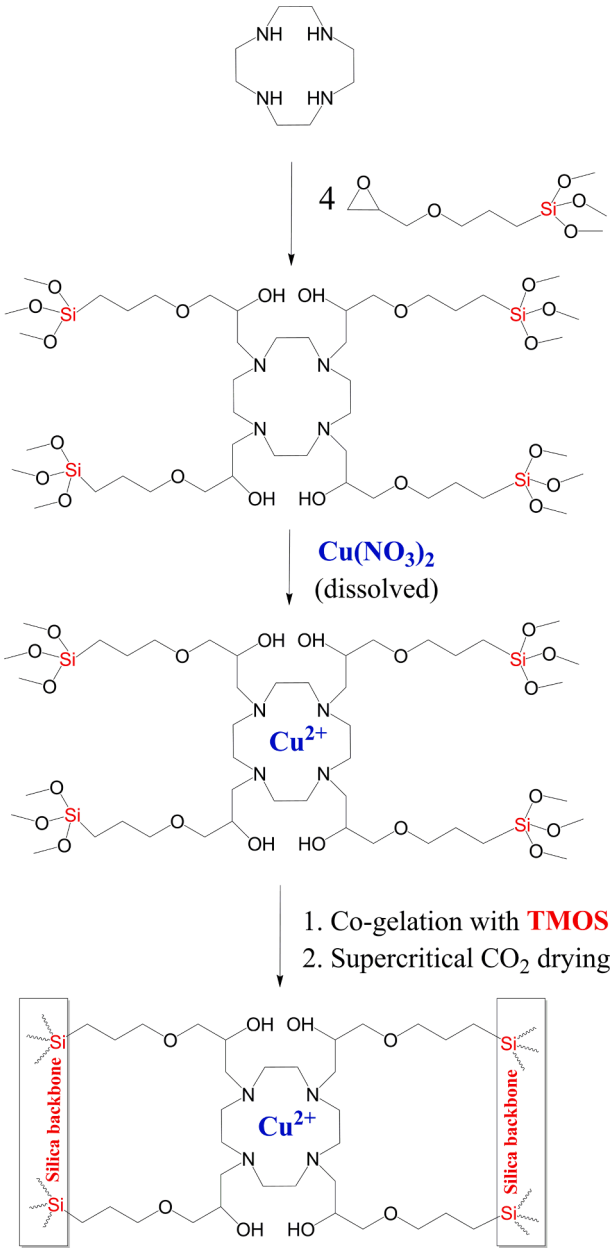

Scheme 1. Synthesis and schematic structure of the Cu(II)-cyclen functionalized silica aerogel, denoted as CuCy-AG.

The steps of the formation of the immobilized Cu(II)-cyclen and the chemical structure of the covalently bound complex are shown in Scheme 1. The resulting pristine Cu(II)-cyclen functionalized aerogel is denoted CuCy-AG through the paper.

2.3. Aerogel characterization

2.3.1. Conventional characterization techniques

The morphology of the aerogel was studied by low voltage scanning electron microscopy (LV SEM) with a ThermoFisher Scientific Scios 2 instrument. The sample was fixed with a vacuum-resistant carbon tape on the sample holder. Because of the low accelerating voltage and small electron beam current, the charging effects of the aerogel sample were practically eliminated [28]. Therefore, fresh fracture surfaces of the

aerogels were imaged in their pristine states without the application of conductive coatings on the samples.

The apparent (specific) surface area, the pore size distribution and the pore volume of the aerogels were measured by N_2 adsorption–desorption porosimetry (Quantachrome Nova 2000e). The samples were degassed under vacuum at 80 °C for 24 h before the measurements. The apparent surface area was calculated from the adsorption curve using the BET method. The pore size distribution was calculated from the desorption curve using the BJH method.

The infrared spectrum (IR) of the aerogel was measured with Perkin Elmer Spectrum Two Spectrometer in attenuated total reflection (ATR) mode.

2.3.2. Copper content of aerogel

Four sets of experiments were performed to determine the copper content CuCy-AG. In the first two experiments, 10.0 mg powdered CuCy-AG was soaked in 4.00 ml of ultrapure water for 8 h and another 10.0 mg CuCy-AG in 0.01 M HNO_3 solution for 1 h. In the third experiment, a mixture of 4.00 ml of 65% HNO_3 and 1.00 ml of 30% H_2O_2 solutions were added to 10.0 mg powdered CuCy-AG and heated in a Milestone EHTOS UP high-power microwave digestion system. In the microwave digestion system, the reaction mixture was heated to 200 °C in 15 min, and kept at high temperature for another 15 min. In the fourth experiment, the reaction conditions were the same as in the third experiment, but an additional 1.00 ml of 40% HF solution was added to the reaction mixture for digestion. After cooling, 1.00 ml of 45 g/L boric acid solution was added to the fourth sample, and heated again to 160 °C for 10 min. The digested samples were brought to 25.0 ml final volume by ultrapure water, and by 20 g/L boric acid solution in the case of the fourth sample. In the case of the first three experiments, the silica residues were removed by centrifugation. In the fourth experiment, CuCy-AG was completely solubilized.

The copper content was measured by ICP-OES technique using an Agilent 5100 SVDV spectrometer. Five point matrix fitted calibration was applied, diluted from 1000 mg/L standard solution (Scharlau) and the intensity values were collected at 327.395 nm. Measurements of each sample were repeated three times. Measuring parameters were as follows: read time: 5 s; uptake delay: 15 s; rinse time: 30 s; stabilization time: 10 s, viewing height: 8 mm, the nebulizer gas flow rate: 0.70 L/min, plasma gas flow rate: 12.0 L/min. SVDV viewing mode was applied. The concentrations of at least 3 parallel samples were averaged.

2.3.3. Small angle neutron scattering (SANS)

SANS experiments were performed on the Yellow Submarine instrument available at Budapest Neutron Center. This is a pin-hole type instrument with a two-dimensional neutron detector. Two sample-to-detector distances (1.2 m and 5.4 m) and two wavelengths (4.38 Å and 10.23 Å) were used. The beam diameter was 8.0 mm. The samples were measured for 60 – 180 min at room temperature. The momentum transfer (Q) is defined by the following equation:

$$Q = \frac{4\pi}{\lambda}\sin\frac{\theta}{2} \tag{1}$$

Here, λ is the wavelength of the monochromatic neutron beam and Θ is the scattering angle. By altering λ and sample-detector distance, a Q range of 0.0065 – 0.4000 $Å^{-1}$ was covered. The definition of the scattering intensity (I) is as follows:

$$I(\lambda,\theta) = I_0(\lambda)\Delta\Omega\eta(\lambda)TV\frac{d\Sigma}{d\Omega}(Q) \tag{2}$$

Here, I_0 is the incoming neutron flux, $\Delta\Omega$ is the unit solid angle, $\eta(\lambda)$is the detector efficiency, T and V are the transmission and volume of the sample and $\frac{d\Sigma}{d\Omega}(Q)$ is the macroscopic differential cross section. The macroscopic differential cross section conveys structural information on the studied system. The measured scattering intensity was corrected for sample transmission, empty cell scattering, solvent scattering, detector sensitivity and background scattering.

The structural parameters of the scattering objects were determined by the mathematical analysis of the corrected $I(Q)$ curves. For a wide Q range where both the Guinier and the Porod approximations can be used for different parts of the SANS curve, their combination is applicable. This is referred to as the Beaucage model, and it covers the whole Q range [29,30].

$$I(Q) \cong A\exp\left(-\frac{Q^2Rg^2}{3}\right) + B\left\{\frac{\left[\mathrm{erf}\left(\frac{QR_g}{\sqrt{6}}\right)\right]^3}{Q}\right\}^{-p} \tag{3}$$

R_g is the average gyration radius, p is the power exponent, and A and B are coefficients related to the volume and number density of the scattering objects and to their contrast. Parameters A and B can be treated as adjustable scaling parameters. Data fitting was performed by using non-linear least-squares algorithms in the Igor Pro 6.1 software.

Dry, powdered CuCy-AG was introduced into 2.0 mm thick quartz cuvettes. The aerogel was measured both in its pristine state, and filled with a liquid in order vary the contrast in the sample. Measurements were made when the aerogel was filled with H_2O, D_2O or a H_2O – D_2O mixture in the composition of 66 (V/V)% H_2O – 34 (V/V)% D_2O. The liquid to dry aerogel mass ratio was 4.0 g/g in each sample. After gentle homogenization, the filled samples were stored overnight at room temperature before SANS measurements.

2.3.4. Electron spin resonance (EPR) spectroscopy

Copper(II)-cyclen complex and $CuCl_2$ were investigated in aqueous solution. Copper(II)-cyclen functionalized aerogel was investigated in its dry state as a powder and in aqueous suspension. X-band CW-EPR spectra were recorded with a BRUKER EleXsys E500 spectrometer (microwave frequency 9.4 GHz, microwave power 13 mW, modulation amplitude 5 G, modulation frequency 100 kHz). For the frozen solution measurements, an 0.2 ml aliquot of Cu(II)-cyclen sample was introduced into a quartz EPR tube then 0.05 ml MeOH was added to avoid the crystallization of water. The EPR tubes were placed into a Dewar container filled with liquid nitrogen at 77 K. For powder EPR measurements in the case of the dry aerogel, the spectra were recorded at room temperature.

The measured spectra were corrected by the baseline spectrum measured in the same way and simulated using a designated EPR program [31]. Axial $\boldsymbol{g}$-tensor ($g_\parallel$ and $g\perp$) and copper hyperfine $\boldsymbol{A}$-tensor ($A_\parallel$ and $A\perp$) have been used for the simulation of the components. The super-hyperfine coupling of the coordinated nitrogen atoms is not resolved in the spectra. The linewidths were fitted by using axial linewidth parameters ($\omega\parallel$,$\omega\perp$). Since a natural $CuCl_2$ was used for the measurements, the spectra were calculated as the sum of the spectra of ^{63}Cu and ^{65}Cu weighted by their natural abundances. The copper and nitrogen coupling constants and the relaxation parameters were obtained in field units (Gauss = 10^{-4} T).

2.4. Catalytic oxidation of phenol

2.4.1. Kinetic measurements by on-line UV–vis spectrophotometry

The catalytic oxidation of phenol was monitored by on-line UV–vis spectrophotometry using a fiber optic spectrophotometer (AvaLigh-DHc lamp and Avantes Avaspec-2048L-TEC-RS detector) [32]. The reactions for these measurements were typically run in 10 mm × 10 mm standard spectrophotometric cuvettes constantly stirred by a built-in magnetic stirrer. A built-in Peltier unit ensured temperature control. The volume of the reaction mixture was 3.00 ml, the temperature was 70 °C and the reaction mixture was stirred at 700 rpm. The progress of the reaction was monitored as a function of time in the wavelength range between 200 and 1000 nm. Spectra were recorded in short intervals (0.5 – 2.0 min) in order to get at least 500 time resolved spectra for one reaction

[33].

When larger reaction volumes were needed for external instrumental analysis, the kinetic experiments were run in stirred reactors, under identical conditions. The progress of these reactions was also monitored by UV–vis spectrophotometry by taking samples.

The concentration of the CuCy-AG catalyst was typically 0.113 mg mL^{-1} which corresponds to 27.3 μM Cu(II)-cyclen. The catalyst concentration used in homogeneous reactions was the same. In order to prepare Cu(II)-cyclen solution without free Cu^{2+} ions, free cyclen was used in 1.0% excess over Cu(II). The typical initial concentration (c_0) of phenol was between 1.00 and 20.0 mM, and that of H_2O_2 was between 50.0 and 500 mM. The concentration of the H_2O_2 stock solution was standardized by iodometric titration. The concentration and the purity of phenol solutions were measured by capillary electrophoresis.

The reaction mixtures were not buffered, and the pH of the reaction mixture was measured with a Metrohm 913 pH meter equipped with an 6.0234.100 pH-electrode [34].

2.4.2. Analysis of the reaction mixture by capillary electrophoresis (CE)

The progress of the reactions was monitored both in the homogeneous and in the heterogeneous systems by micellar electrokinetic capillary chromatography (MEKC), which is one of the techniques of capillary electrophoresis (CE). MEKC can be especially useful for the determination of uncharged / hydrophobic / slightly water soluble compounds. The surfactant sodium dodecyl sulfate (SDS) formed micelles. The different partitioning of phenols between the aqueous the background electrolyte and the hydrophobic micellar phase is the basis for separation.

Kinetic experiments were conducted under the same conditions as for on-line UV–vis detection, but in larger volume. Samples were collected from the reaction mixtures and immediately frozen in order to stop the reaction. The samples were melted at 15 °C before analysis. (The reactions were still practically halted at 15 °C.)

The MEKC experiments were carried out on an Agilent 7100 capillary electrophoresis device (Agilent, Waldbronn, Germany). The electropherograms were recorded and processed by ChemStation computer program of B.04.02 version (Agilent). Separations were performed using polyimide coated fused-silica capillaries of 65 cm 50 mm id (Polymicro Technology, Phoenix, AZ, USA). The 2–3 mm window for detecting was prepared with the burning of the polyimide layer. The capillary was conditioned for 15 min with a 1.0 M NaOH solution before the first use, then with a 0.1 M NaOH solution for 30 min and finally with the buffer solution for 30 min. Before the measurements, the capillary was conditioned with the buffer solution for 5 min. The following experimental conditions were used during the measurements: l_t = 65 cm, 50 mM phosphate, 50 mM SDS, pH = 7.0, +20 kV, +50 mbar × 2 sec, λ = 210 nm. UV–vis spectra were recorded under the same measurement conditions by a diode-array detector. The chemical components of the reaction mixtures were identified based on migration time spiking the sample with standards, and based on their UV–vis spectra compared to those of the standards.

3. Results and discussion

3.1. Morphology and pore structure of CuCy-AG

3.1.1. Scanning electron microscopy (SEM)

Representative SEM images of the CuCy-AG are shown in Fig. 1. The functionalized aerogel is built from primary spherical nanoparticles interconnected to form an open porous network, which is typical for silica aerogels. The structure contains mostly mesopores of quasi-spherical shape. Additionally, a few macropores (d_{pore} = 150 – 200 nm) are visible in the images. There are no aggregated clusters or ridges visible in SEM pictures, which indicates that the nanoscale structure of the aerogel is uniform resulting in a consistent morphology. Overall, the incorporation of Cu(II)-cyclen does not alter the fundamental morphology of the aerogel compared to that of archetypical silica aerogels, which is desirable [35].

3.1.2. N_2–sorption porosimetry

Nitrogen adsorption–desorption isotherms of CuCy-AG are shown in Fig. 2. The hysteresis curve is classified as IUPAC IV category with a H3 type loop. This is characteristic for mesoporous materials with a small number of macropores [36]. According to the *t*-plot method, the contribution of micropores is also negligible to the total porosity [37]. Pore size distribution calculated using the BJH method are shown in Fig. 2. The structural parameters calculated form the sorption isotherms are collected in Table 1. As a reference, the structural parameters of the parent archetypical silica aerogel are also shown in Table 1. The apparent surface area of CuCy-AG is 464 m^2/g, which is relatively low for silica aerogels. The mean pore size was estimated to be 31 nm. The results of the N_2-sorption porosimetry indicate, that the pore structure of silica aerogel is somewhat altered as a consequence of the incorporation of Cu(II)-cyclen. The apparent surface area and the total mesopore volume of CuCy-AG are lower, and the mean pore size is larger compared to those of archetypical silica aerogel. The reason can be that the relative rates of the hydrolysis and polycondensation reactions yielding the silica network are altered due to the presence of the Cu(II) containing precursor, that in turn result in a somewhat altered pore architecture [38].

3.1.3. Infrared spectroscopy (IR)

The representative FT-IR spectrum of the CuCy-AG is shown in Fig. 3. An intense broad band was observed at 1050 cm^{-1} that is typical for silica aerogels. This band is assigned as the Si–O–Si antisymmetric stretching vibration. At 2870 and 2950 cm^{-1}, two weak bands are

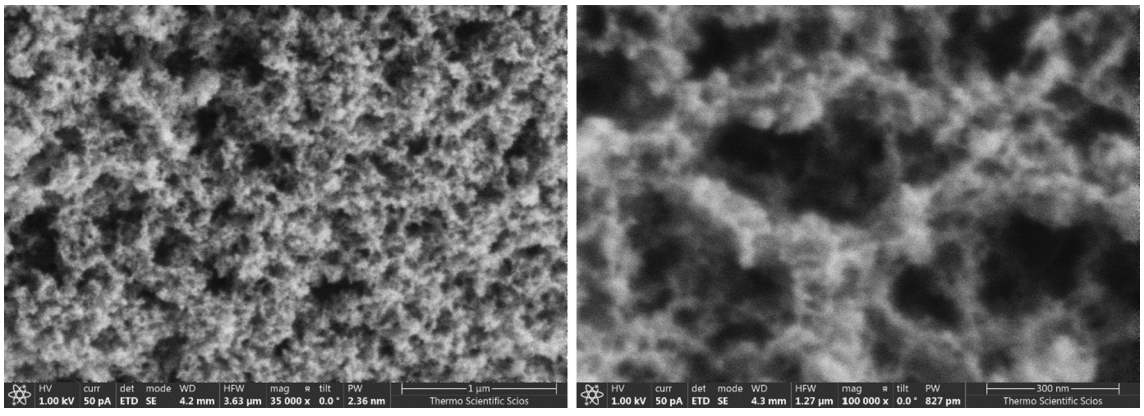

Fig. 1. Scanning electron microscopy (SEM) images of CuCy-AG in 35 k× (left) and 100 k × magnification (right).

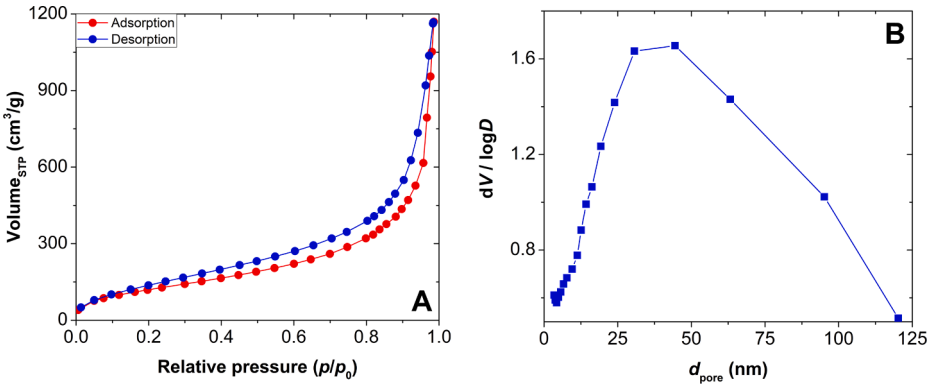

Fig. 2. Panel A: Nitrogen adsorption (red) and desorption (blue) isotherms of the CuCy-AG. Panel B: Pore size distribution calculated from the desorption isotherm using the BJH method.

Table 1
Structural parameters of Cu(II)-cyclen and pure silica aerogel estimated by the BET and the BJH methods from N_2 adsorption–desorption porosimetry data [39].

Parameter	CuCy-AG	silica aerogel	Data evaluation
C-constant	35	70	BET
Apparent surface area (m^2/g)	464	768	BET
Average pore size (nm)	31	25	BJH
Total pore volume (cm^3/g)	3.7	6.0	BJH

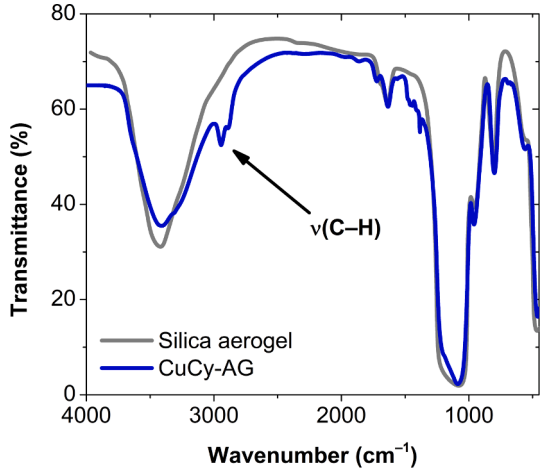

Fig. 3. Infrared spectra (FT-IR) of the pristine CuCy-AG and the parent silica aerogel.

present that are not detectable in the parent silica aerogel. These peaks are attributed to aliphatic C–H stretching vibrations, and certainly arise due to the functionalization with the Cu(II)-cyclen complex. The IR data are in excellent agreement with those of published in the article first describing the synthesis of CuCy-AG [25].

3.2. Copper content of CuCy-AG

In order to determine the copper content of CuCy-AG, ICP-OES measurements were carried out using different sample preparation strategies (cf. Section 2.3.2). After soaking CuCy-AG in ultrapure water, no copper was detected in the resulting solution. When CuCy-AG was soaked in 0.01 M HNO_3, the amount of solubilized copper corresponded to 0.42 wt% of the aerogel. The amount of solubilized copper was 1.53 wt% using microwave digestion without HF, while adding HF increased this value to 1.59 wt%.

Soaking in water did not liberate any copper from CuCy-AG; meaning there is no weakly bound dissolvable Cu(II) in the functionalized aerogel. If the Cu(II)-cyclen is not bound by multiple covalent bonds to the silica backbone (cf. Scheme 1), dilute nitric acid can hydrolyze the linkage and solubilize the complex. This is operative only for a fraction of Cu(II)-cyclen in the aerogel. Microwave digestion without HF completely destroys the organic part of the aerogel, but not the silica framework; while digestion with HF completely solubilizes CuCy-AG. Complete solubilization corresponds to 1.59 wt% copper content. Therefore, this value was used in further calculations.

3.3. Small angle neutron scattering (SANS)

Representative SANS curves measured for the pristine and the filled CuCy-AG samples are shown in Fig. 4. The SANS curves of the pristine and the H_2O or D_2O filled CuCy-AG samples are structured, and can be fitted using the Beaucage model. The goodness of the fit of these curves were better when the Beaucage model was complemented with a second power-law component. The estimated values of the gyration radius (*Rg*) and the power exponents (p_1 and p_2) are given in Table 2. Pore size was calculated from the gyration radius assuming the spherical geometry of pores [29,40].

The neutron scattering length density (SLD) of amorphous silica is 1.96×10^{-6} Å^{-2}, which is expected to be matched by filling the aerogel with the 66 (V/V)% H_2O – 34 (V/V)% D_2O (64 wt% H_2O – 36 wt% D_2O)

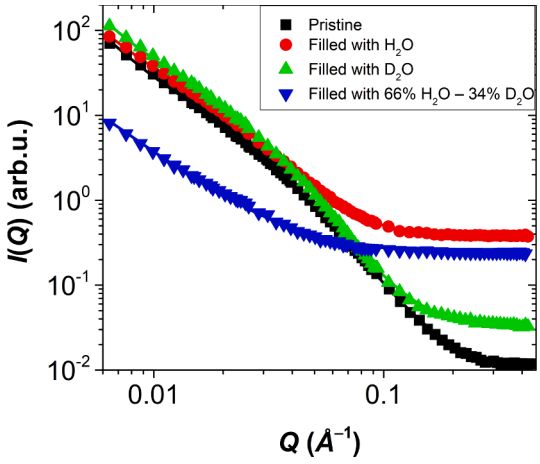

Fig. 4. Small angle neutron scattering (SANS) curves of CuCy-AG measured in its pristine state and filled with H_2O, D_2O or a H_2O-D_2O mixture, as indicated in the legend. Markers are experimental data points and continuous lines are results of non-linear fitting. The estimated structural parameters are given in Table 2.

Table 2
Structural parameters estimated by fitting the SANS curves of the pristine and the filled aerogel samples with the Beaucage or the power-law model. The experimental SANS curves and the non-linear fits are shown in Fig. 4.

Sample preparation	Beaucage + power-law model R_g (Å)	d_{pore} (nm)	Beaucage + power-law model p_1	Beaucage + power-law model p_2	Power-law model p
Pristine	86 ± 3	22	2.8 ± 0.1	3.5 ± 0.1	
H_2O	95 ± 4	25	2.6 ± 0.1	3.5 ± 0.2	
D_2O	97 ± 3	25	2.9 ± 0.1	3.8 ± 0.1	
H_2O – D_2O					1.9 ± 0.1

mixture [41,42]. Indeed, the corresponding SANS curve shows practically no specific scattering due to the contrast of nanosized objects. This curve can be fitted only with a single power-law scattering model, which yields a single p value (Table 2).

The average pore diameter of CuCy-AG is 22 nm according to SANS, which is in reasonable agreement with the pore size distribution calculated from N_2-sorption data. The $p_1 = 2.8$ value for the pristine aerogel is characteristic for mass fractals that is in agreement with the fundamental morphology of silica aerogels [38]. The second power-law exponent $p_2 = 3.5$ is characteristic for surface fractals. The presence of the second Porod region is reasonble due to the presence of macropores in the aerogel. Scattering on the nanostructured surface of the large macropores are assumed to be responsible for the surface-fractal type Porod region.

The fact that the contrast of CuCy-AG can be matched by the estimated H_2O – D_2O mixture is a strong indication that the Cu(II)-cyclen moieties do not form nanosized clusters in the functionalized aerogel. In the case of the aggregation of the Cu(II) containing structural elements, they would be expected to show marked specific scattering when the contrast of silica is matched. Accordingly, the contrast variation SANS result suggest that the Cu(II)-cyclen moieties are dispersed homogeneously in the functionalized silica aerogel. This idea is further strengthened by the EPR results, as detailed later.

3.4. EPR spectroscopy

Electron spin resonance (EPR) spectroscopy measurements were carried out in order to investigate the coordination mode of the Cu(II)-cyclen complex in CuCy-AG. The solution of Cu(II)-cyclen was investigated frozen at 77 K. The EPR spectrum of pristine CuCy-AG was recorded in its dry state, and that of the hydrated CuCy-AG was recorded in aqueous suspension frozen at 77 K (Fig. 5).

The frozen solution spectrum of Cu(II)-cyclen complex features an exclusive copper(II) species (Component 1) characterized by an axial $\boldsymbol{g}$-tensor (Table 3). The obtained EPR parameters slightly differ from those reported previously for Cu(II)-cyclen complexes, but they fall within the margin of error [43,44]. For the dry and the wet CuCy-AG systems, the EPR spectra cannot be assigned to one axial $\boldsymbol{g}$-tensor, and the parameters can be fitted well only if two components were considered (Component 2 and 3).

In the case of Component 2, the $\boldsymbol{g}$- and $\boldsymbol{A}$-tensors are similar to those obtained for Component 1. This component exhibits significant line broadening ($\omega_\perp$, $\omega_\parallel$ values) which can be readily explained by considering the fact, that the copper centers in the aerogel are relatively close and the dipole–dipole interactions between them is able to increase the line broadening. However, the interaction between the two unpaired electrons (e.g. the distance between the Cu(II) centers) is not strong enough to cause antiferromagnetic coupling.

The parameters of Component 3 differ significantly from those of Component 1 and 2. The large $g_\parallel$ and small $A_\parallel$ values corroborate the presence of weaker equatorial ligand field in this component. Such complex can be envisioned when one of the nitrogen atoms is not bound

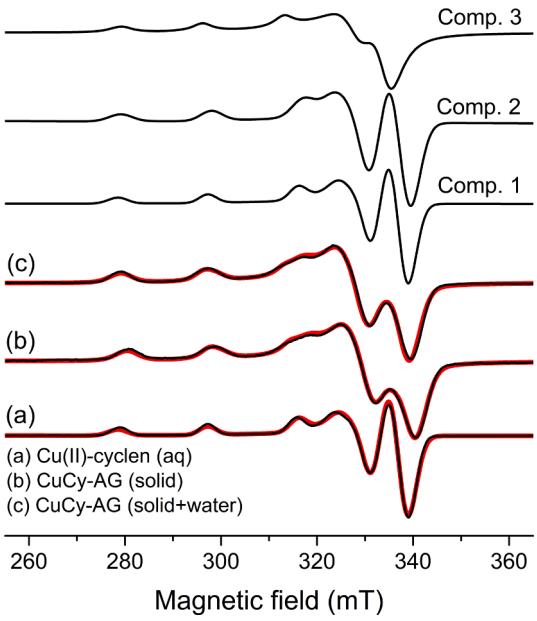

Fig. 5. Experimental (black) and simulated (red) EPR spectra recorded for the frozen solution of Cu(II)-cyclen complex (a); the dry CuCy-AG aerogel (b) and the frozen suspension of the wet aerogel (c). The component spectra obtained in the simulations are shown as follows. Spectrum (a) was fitted with Comp. 1 in 100%, spectrum (b) with 54% Comp. 2 + 46% Comp. 3 and (c) with 62% Comp. 2 + 38% Comp. 3.

Table 3
Anisotropic EPR parameters obtained in the simulation of the recorded EPR spectra. Coupling values and linewidth parameters are in units of 10^{-4} cm^{-1}.[a]

	$g_\perp$	$g_\parallel$	$A_\perp$	$A_\parallel$	$\omega_\perp$	$\omega_\parallel$
Comp.1	2.044	2.197	16	190	20	18
Comp.2	2.049	2.194	17	190	23	22
Comp.3	2.056	2.211	10	171	37	25

[a] The experimental error was ± 0.001 for $g_\perp$ and $g_\parallel$; ±1 × 10^{-4} cm^{-1} for couplings and linewidth parameters.

in the equatorial plane, or the copper(II) is accommodated by the binding of the hydroxyl group of the linker in the axial position. The ratio of the Component 3 decreases when water is added to the sample. This is most probably due to the presence of a metastable H-bond network in the dry state. Thus, it is reasonable to assume that the supercritical drying conserves metastable conditions. The addition of water to the aerogel breaks the conserved structure and shifts the metastable condition to the thermodynamically stable state.

3.5. Mechanism of catalytic oxidation of phenol

3.5.1. Reaction intermediates

Both the homogeneous and the heterogeneous reactions were followed on-line in high time resolution by UV–vis spectrophotometry. The spectral changes correspond to the depletion of phenol, the concerted formation of multiple reaction intermediates, and finally, the depletion of these intermediates (Fig. 6) [25].

In order to identify the intermediates, samples were withdrawn from the reaction mixtures and analyzed using CE-MEKC. Four major intermediates were identified in the case of both the homogeneous and heterogeneous reaction mixtures: 1,2-dihydroxybenzene (*1,2*-DH); 1,4-dihydroxybenzene (*1,4*-DH); 1,2-benzoquinone (*1,2*-BQ) and 1,4-benzoquinone (*1,4*-BQ) (Representative electropherograms of standards and reaction mixtures are shown in the Supporting Information). In general, the concentrations of *1,2*-DH, *1,4*-DH and *1,2*-BQ are much higher in the

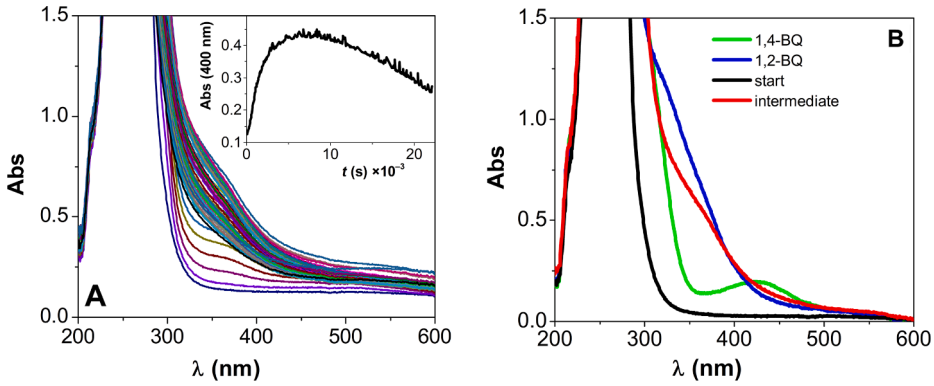

Fig. 6. Panel A: Time resolved spectra recorded during the catalytic oxidation of phenol in the presence of CuCy-AG. Inset: kinetic curve at 400 nm (c_0(phenol) = 4.3 mM; $c_0(H_2O_2)$ = 300 mM; $c_{catalyst}$ = 0.027 mM; 70 °C). Panel B: UV–vis spectra of *1,2*-BQ (blue) and *1,4*-BQ (green) superimposed on the baseline corrected spectrum of the mixed reactants (black) and the spectrum of the reaction mixture when the intermediates are present at maximum concentration levels (red).

reaction mixtures than that of *1,4*-BQ. The variation of the integral of the CE-MEKC peaks of the intermediates as a function of reaction time is in good agreement with the kinetic curves recorded by on-line spectrophotometry (Fig. 7). According to the CE-MEKC measurements, the accumulation of *1,2*-DH, *1,4*-DH and *1,2*-BQ is well-expressed in both reaction systems at high initial concentrations of phenol, but the kinetics of their production and subsequent oxidations are different. These kinetic phenomena will be discussed in Section 3.5.2. The oxidation of the benzoquinones results in ring-opening and the formation of a mixture of dicarboxylic acids. The same oxidation intermediates and products were identified by HPLC in a study published earlier [25].

The UV–vis spectra of the reaction mixtures recorded at intermediate reaction times are characteristic for the intermediates. These spectra are in excellent agreement with that of *1,2*-BQ in the case of both the homogeneous and heterogeneous reactions (Fig. 6). However, matrix rank analysis of the time resolved UV–vis spectra suggests the presence of two light absorbing intermediates (Table S1 in the Supporting Information). Therefore, besides *1,2*-BQ, the minor contribution of *1,4*-BQ is also observed in the time resolved UV–vis spectra both in the heterogeneous and homogeneous reactions.

Independent measurements confirm that the pH values of the reaction mixtures change in time due to the formation of dicarboxylic acid products. The starting pH is between 4.4 and 5.6 depending on the initial concentrations of phenol and H_2O_2. The final pH after the oxidation of the DH and BQ intermediates is between 3.1 and 3.3 depending on the conditions of the kinetic experiments.

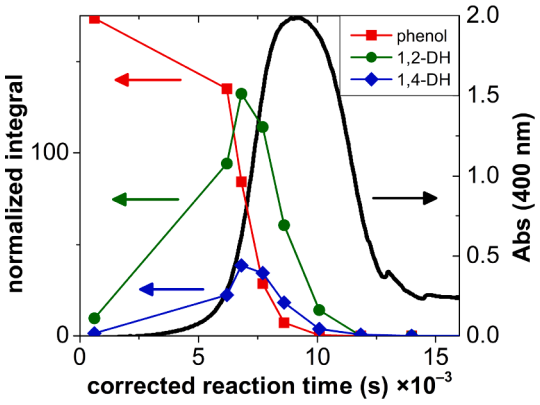

Fig. 7. The variation of the integrals of the CE-MEKC peaks of phenol and dihydroxybenzene intermediates as a function of reaction time superimposed on the kinetic curve recorded by UV–vis spectrophotometry. (c_0(phenol) = 20 mM; $c_0(H_2O_2)$ = 300 mM; $c_{catalyst}$ = 0.136 mM; 70 °C; λ = 400 nm).

3.5.2. Kinetic model

The catalyst concentrations were calculated based on Cu(II) contents both in the homogenous and heterogeneous reaction systems. This was standardized using elemental analysis by ICP-OES. Thus, equivalent catalyst concentrations means the equivalent concentrations of the Cu (II)-cyclen, either dissolved or immobilized in CuCy-AG.

For the quantitative evaluation of the time resolved UV–vis spectra in a kinetic run, we had to take into account that CuCy-AG is present as a suspension in the heterogeneous reaction mixture. In these experiments, light scattering from the aerogel caused the slight elevation of the baseline of the UV–vis spectra. This effect was corrected using the dual-wavelength method as described by Liu and Zhu, i.e. the subtraction of the apparent absorbance (extinction) of the aerogel suspension from the UV–vis spectra at each reaction time [45,46]. In the case of the homogeneous Cu(II)-cyclen catalyst, no such correction is required.

Informative kinetic curves can be constructed by plotting the absorbance at 400 nm as a function of reaction time. At this wavelength, only the *1,2*-BQ and *1,4*-BQ intermediates absorb light. Thus, the kinetic curves start at zero absorbance, and return to zero absorbance by the oxidation of the intermediates. Representative kinetic curves are shown in Fig. 8 demonstrating the effect of the variation of the concentration of the catalyst. Additional kinetic curves showing the effects of the variation of the initial concentrations of phenol and H_2O_2 are reported in the Supporting Information (Figs. S1 – S3). A short induction period is present in some of the kinetic curves. A semi-quantitative observation is that oxidation of phenol and the concerted formation of the intermediates are faster using heterogeneous CuCy-AG catalyst. On the other hand, the subsequent oxidation of the intermediates is significantly faster in the presence of dissolved Cu(II)-cyclen.

The simplest kinetic model that adequately describes the reaction systems is given in Scheme 2. This model provides a coherent mechanistic interpretation of the experimental observations. The proposed reaction steps (from R1 to R12) are the same for the homogeneous and the heterogeneous systems. All reaction steps are second order. The first step (R1) is the direct reaction of H_2O_2 with Cu(II)-cyclen yielding an active intermediate (CuCat*). Based on the works of Robbins et al. and others, this activation step is proposed to involve the formation of a Cu (II)-hydroperoxide complex [47–49]. This elementary reaction step is of key importance in the kinetic model, because this is naturally the first step in the catalytic cycle. Once formed, the CuCat* species is proposed to react rapidly with organic compounds. The active catalyst (CuCat*) might oxidize H_2O_2 to O_2 (R2), which is a side reaction to be considered [50]. The catalytic oxidation of phenol (Phe) by CuCat* to *1,2*-DH and *1,4*-DH takes place in reactions R3 and R4, respectively. The catalytic oxidation of the dihydroxybenzenes takes place in two consecutive reaction steps. First, they are oxidized to the corresponding quinones (R7 and R8); and in subsequent steps, the quinones are oxidized to products

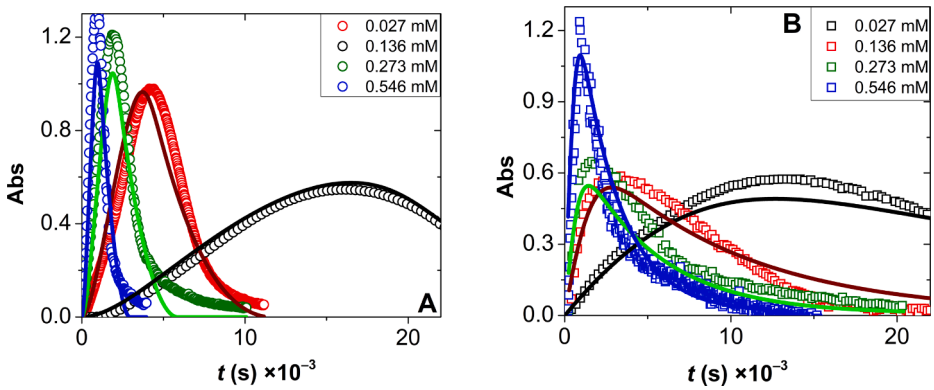

Fig. 8. Kinetic curves recorded at different catalyst concentrations in the homogeneous (A) and heterogeneous (B) reactions. Markers: measured data. Lines: results of global fitting using the kinetic model of Scheme 2. c_0(phenol) = 4.3 mM; $c_0(H_2O_2)$ = 300 mM; $c_{catalyst}$ = 0.027 – 0.546 mM; 70 °C.

			Heterogeneous	Homogeneous
R1	2 CuCat + H_2O_2 → 2 CuCat*	k_1 ($M^{-1}s^{-1}$)	$(7.4 \pm 0.4)\times10^{-2}$	$(2.3 \pm 0.1)\times10^{-2}$
R2	2 CuCat* + H_2O_2 → 2 CuCat + O_2	k_2 ($M^{-1}s^{-1}$)	$< 10^{-5}$	$< 10^{-5}$
R3	CuCat* + Phe → *1,2*-DH + CuCat	k_3 ($M^{-1}s^{-1}$)	$(1.1 \pm 0.2)\times10^{0}$	$(7.1 \pm 0.7)\times10^{3}$
R4	CuCat* + Phe → *1,4*-DH + CuCat	k_4 ($M^{-1}s^{-1}$)	$(9.1 \pm 0.3)\times10^{0}$	$(2.6 \pm 0.2)\times10^{4}$
R5	*1,2*-DH + H_2O_2 → *1,2*-BQ	k_5 ($M^{-1}s^{-1}$)	$< 10^{-5}$	
R6	*1,4*-DH + H_2O_2 → *1,4*-BQ	k_6 ($M^{-1}s^{-1}$)	$< 10^{-5}$	
R7	*1,2*-DH + 2 CuCat* → *1,2*-BQ + 2 CuCat	k_7 ($M^{-1}s^{-1}$)	$> 10^{4}$	$> 10^{4}$
R8	*1,4*-DH + 2 CuCat* → *1,4*-BQ + 2 CuCat	k_8 ($M^{-1}s^{-1}$)	$< 10^{1}$	$< 10^{1}$
R9	*1,2*-BQ + H_2O_2 → $Prod_1$	k_9 ($M^{-1}s^{-1}$)	$< 10^{-4}$	
R10	*1,4*-BQ + H_2O_2 → $Prod_2$	k_{10} ($M^{-1}s^{-1}$)	$< 10^{-5}$	
R11	*1,2*-BQ + 2 CuCat* → $Prod_1$ + 2 CuCat	k_{11} ($M^{-1}s^{-1}$)	$(6.7 \pm 0.2)\times10^{0}$	$(2.0 \pm 0.5)\times10^{3}$
R12	*1,4*-BQ + 2 CuCat* → $Prod_2$ + 2 CuCat	k_{12} ($M^{-1}s^{-1}$)	$> 10^{0}$	$> 10^{3}$

Scheme 2. Kinetic model for the catalytic oxidation of phenol. All reaction steps are second order and the rate constants are in the unit of M^{-1} s^{-1}. The complete system of rate equations derived from the kinetic model is given in the Supporting Information. The rate constants were estimated by global data fitting including multiple experimental kinetic curves representing the variation of the initial concentrations of the catalysts, H_2O_2 and phenol ($c_{catalyst}$ = 0.027 – 0.546 mM; c_0(phenol) = 1.0 – 5.7 mM; $c_0(H_2O_2)$ = 200 – 500 mM). Calculated kinetic curves are shown in Figs. 8 and 9. [Abbreviations: CuCat: catalyst, CuCat*: activated catalyst, Phe: phenol, Prod: product].

(R11 and R12). The direct reactions between H_2O_2 and the dihydroxybenzenes (R5 and R6) and the analogous non-catalyzed oxidation of the quinones (R9 and R10) are also included in the kinetic model.

A general nature of multistep reaction systems is that the absolute rate of a reaction step that consumes an intermediate cannot be higher than the rate of the step producing this intermediate, because the concentration of the intermediate would otherwise drop to very small values rapidly halting the reaction. In the studied systems, CuCat* is present as a steady-state intermediate under both heterogeneous and homogeneous conditions, and the rate of Phe degradation is determined by the interplay of several kinetically coupled reaction steps. Therefore, we refrained from using any approximations and applied the approach of global kinetic data fitting and simulation [51]. The complete system of rate equations derived from the kinetic model of Scheme 2 and used for the computations is given in the Supporting Information. Global data fitting was performed using the kinetic curves recorded by UV–vis spectrophotometry. Multiple sets of kinetic curves recorded under different initial conditions were simultaneously evaluated with the program package ZiTa using the GEAR algorithm [52]. From the two reaction systems, a selection of 8 – 8 kinetic curves were included in the global evaluation in the initial concentration range of $c_{catalyst}$ = 0.027 – 0.546 mM; c_0(phenol) = 1.0 – 5.7 mM; $c_0(H_2O_2)$ = 200 – 500 mM. The molar absorbances of phenol, *1,2*-DH, *1,4*-DH and the products were considered zero at λ = 400 nm. The molar absorbances of *1,2*-BQ and *1,4*-BQ were determined independently and were fixed parameters in the calculations. The initial values of all rate constants were varied in a systematic way in order to sensitize the optimizing algorithm to all reaction steps. As seen in Fig. 8, satisfactory results were obtained in the selected range of initial concentrations. The estimated rate constants are listed in Scheme 2; and Fig. 9 shows the calculated concentrations of

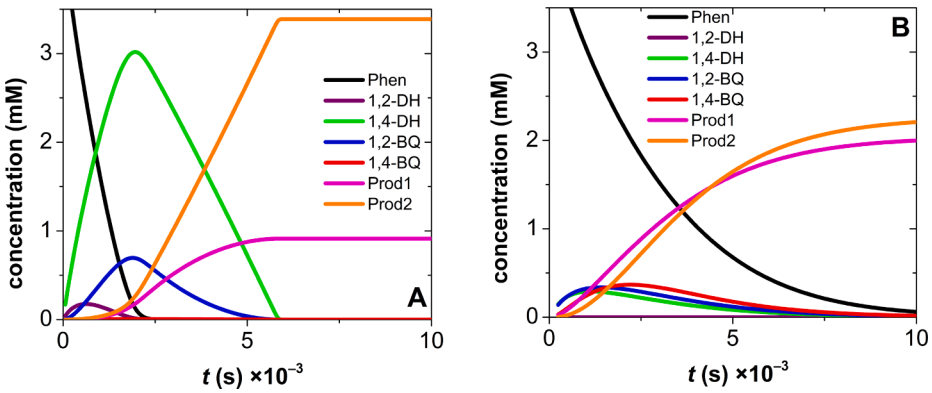

Fig. 9. Calculated concentrations of phenol, the intermediates and the oxidation products as function of reaction time using the same initial concentrations of the reactants in the homogeneous (A) and heterogeneous (B) systems. The calculations are based on the results of global fitting using the kinetic model of Scheme 2. The experimental and the fitted UV–vis kinetic curves are shown in Fig. 8 (green markers and lines). c_0(phenol) = 4.3 mM; $c_0(H_2O_2)$ = 300 mM; $c_{catalyst}$ = 0.273 mM; 70 °C.

phenol, the intermediates and the oxidation products as function of reaction time in representative cases.

In general, the oxidation of phenol and the intermediates display very distinctive kinetics in the two systems. Most of the catalytic reactions are faster in the presence of the homogeneous catalyst, but some trends are similar in the rate constants of the analogous reactions. The oxidation of phenol to *1,4*-DH (R4) is significantly faster than the formation of *1,2*-DH (R3) in both the heterogeneous and the homogeneous systems. However, the subsequent oxidation of *1,4*-DH to *1,4*-BQ (R8) is significantly slower than the oxidation of *1,2*-DH to *1,2*-BQ (R7). Finally, the overoxidation of *1,4*-BQ (R12) is faster than that of *1,2*-BQ (R11) in both systems. These relations result in the accumulation of *1,4*-DH and *1,2*-BQ during the reactions. Depending on the starting concentrations, *1,2*-DH and *1,4*-BQ can also form in detectable transient concentrations, which is in-line with the analytical results discussed in Section 3.5.1.

Earlier reports indicate that *1,2*-DH could reduce a number of Cu(II) compounds to Cu(I) and induce Fenton-like reactions [53]. We considered this possibility and introduced such reaction steps in the global kinetic fitting procedure. The overall result is that neither catalytic systems are sensitive to these reaction steps. The explanation is that the reductions of Cu(II)-complexes are preferred only in highly acidic solutions [53].

3.5.3. *Mechanistic considerations*

The kinetic properties of the heterogeneous reaction system are the consequence of multiple kinetic and mass transport effects. The mass transport (diffusion) of H_2O_2 is practically unhindered in the pores of silica aerogel, similar to that of water, as shown previously by NMR measurements [54]. On the other hand, the diffusion of phenol and its oxidation products are hindered in the pores of the functionalized aerogel. These restricted mass transport processes are reflected in the low rate constants of reactions R3, R4, R11, R12 in the heterogeneous system where phenolic compounds and quinones have to reach the immobilized catalyst inside the pores of the aerogel.

Interestingly, the activation of the catalyst in reaction R1 is faster in the case of the CuCy-AG compared to dissolved Cu-cyclen. The global fitting was very sensitive to the k_1 parameter in both systems, and this parameter is not in correlation with any other. Thus, the difference in k_1 in the two systems is considered significant even in the statistical sense. The higher effective rate constant in the heterogeneous system can be due to the stabilization of Cu(II)-cyclen as the consequence of its immobilization. One effect can be the separation of the copper centers as shown by SANS and EPR, which might inhibit the unwanted interactions of the catalytic centers. Furthermore, the local concentration of H_2O_2 can be elevated inside the pores due to its sorption in silica aerogel, which can also cause the increase of the effective rate constant of the activation of Cu(II)-cyclen situated inside the pores. In addition, the EPR studies confirmed the presence of further Cu(II) species in the aerogel. Here, either the binding of an apical hydroxyl group or a partially occupied equatorial plane is expected. On the basis of earlier studies and plausible considerations, the latter scenario is more likely, thus the equatorial plane of the Cu(II) is expected to contain a displaced solvent (water) molecule [47,48]. This probably provides an easier access for the H_2O_2 and readily yields the active form of the catalyst, i.e. the Cu(II)-hydroperoxide complex. In contrast, the homogenous system unambiguously possesses one exclusive Cu(II) species, wherein all the four equatorial places of Cu(II) are accommodated by the nitrogen atoms of the cyclen moiety. Consequently, the formation of the active form of the catalyst by H_2O_2 (R1) requires the rearrangement of the coordination sphere resulting in lower rate of the activation than in heterogeneous system.

4. Conclusions

Silica aerogel was intended to serve as a chemically inert support for 1,4,7,10-tetraazacyclododecane [Cu(II)-cyclen] as it acts as a catalyst in the oxidation of aqueous phenol by H_2O_2. The morphology of the functionalized aerogel is very similar to that of the parent silica aerogel with an open interconnected mesoporous network. Small angle neutron scattering (SANS) measurements prove that the copper centers are dispersed quasi homogeneously in the silica matrix. There is no indication for the formation of individual copper rich structural regions in the nanometer scale. Electron paramagnetic resonance (EPR) spectroscopy measurements prove, as well, that the Cu(II) centers do not interact with each other, but the coordination mode of Cu(II) is somewhat different than in dissolved Cu(II)-cyclen. Detailed kinetic experiments prove that a unified kinetic model is adequate to describe and benchmark both the homogeneous and the heterogeneous reaction systems. This approach clearly showed that the specific activity of the heterogeneous catalyst is somewhat lower than that of the homogeneous because of hindered mass transport, and not because of ineffective activation or new side reactions. Reflecting to the characterization results highlights that the effective separation of the catalytic centers and the accessible equatorial plane of Cu(II)-cyclen in the functionalized aerogel ensures the conservation of the catalytic activity of the complex. This is naturally advantageous for an immobilized catalyst.

CRediT authorship contribution statement

Attila Forgács: Methodology, Validation, Formal analysis, Investigation, Writing – original draft. **Zoltán Balogh:** Methodology, Validation, Formal analysis, Investigation. **Melinda Andrási:** Methodology, Validation, Formal analysis, Investigation. **Adél Len:** Methodology, Validation, Formal analysis, Investigation. **Zoltán Dudás:** Methodology, Validation, Formal analysis, Investigation. **Nóra V. May:** Methodology, Validation, Formal analysis, Investigation. **Petra Herman:** Methodology, Validation, Formal analysis, Investigation, Writing – original draft, Writing – review & editing, Visualization. **Laura Juhász:** Methodology,

Validation, Formal analysis, Investigation. **István Fábián:** Conceptualization, Resources, Supervision, Funding acquisition. **Norbert Lihi:** Data curation, Writing – original draft, Writing – review & editing, Supervision. **József Kalmár:** Methodology, Validation, Formal analysis, Conceptualization, Validation, Resources, Data curation, Writing – original draft, Writing – review & editing, Supervision.

Declaration of Competing Interest

The authors declare that they have no known competing financial interests or personal relationships that could have appeared to influence the work reported in this paper.

Acknowledgements

We are grateful for Attila Gáspár (University of Debrecen) for his help in the CE measurements. This research has been financially supported by the National Research, Development and Innovation Office, Hungarian Science Foundation (OTKA: FK_17-124571 and K_18-127931). J. Kalmár is grateful for the János Bolyai Research Scholarship of the Hungarian Academy of Sciences and for the New National Excellence Program (ÚNKP-21-5 Bolyai+) of the Ministry of Innovation and Technology of Hungary for financial support. P. Herman is grateful for the New National Excellence Program (ÚNKP-21-4-I).

Appendix A. Supplementary data

Supplementary data to this article can be found online at https://doi.org/10.1016/j.apsusc.2021.152210.

References

[1] R.M. Bruce, J. Santodonato, M.W. Neal, Summary review of the health effects associated with phenol, Toxicol. Ind. Health 3 (4) (1987) 535–568, https://doi.org/10.1177/074823378700300407.
[2] I. Polaert, A.M. Wilhelm, H. Delmas, Phenol wastewater treatment by a two-step adsorption–oxidation process on activated carbon, Chem. Eng. Sci. 57 (9) (2002) 1585–1590, https://doi.org/10.1016/S0009-2509(02)00034-9.
[3] Y. Qu, Q. Ma, J. Deng, W. Shen, X. Zhang, Z. He, J.D.V. Nostrand, J. Zhou, J. Zhou, Responses of microbial communities to single-walled carbon nanotubes in phenol wastewater treatment systems, Environ. Sci. Technol. 49 (7) (2015) 4627–4635, https://doi.org/10.1021/es5053045.
[4] C. Comninellis, A. Nerini, Anodic oxidation of phenol in the presence of NaCl for wastewater treatment, J. Appl. Electrochem. 25 (1995) 23–28, https://doi.org/10.1007/BF00251260.
[5] L.G.C. Villegas, N. Mashhadi, M. Chen, D. Mukherjee, K.E. Taylor, N. Biswas, A short review of techniques for phenol removal from wastewater, Curr. Pollut. Rep. 2 (3) (2016) 157–167, https://doi.org/10.1007/s40726-016-0035-3.
[6] S. Sklavos, G. Gatidou, A.S. Stasinakis, D. Haralambopoulos, Use of solar distillation for olive mill wastewater drying and recovery of polyphenolic compounds, J. Environ. Manage. 162 (2015) 46–52, https://doi.org/10.1016/j.jenvman.2015.07.034.
[7] R. Mukherjee, S. De, Adsorptive removal of phenolic compounds using cellulose acetate phthalate–alumina nanoparticle mixed matrix membrane, J. Hazard. Mater. 265 (2014) 8–19, https://doi.org/10.1016/j.jhazmat.2013.11.012.
[8] C.H. Loh, Y. Zhang, S.W. Goh, R. Wang, A.G. Fane, Composite hollow fiber membranes with different poly (dimethylsiloxane) intrusions into substrate for phenol removal via extractive membrane bioreactor, J. Membr. Sci. 500 (2016) 236–244, https://doi.org/10.1016/j.memsci.2015.12.001.
[9] X. Guan, D.i. He, J. Ma, G. Chen, Application of permanganate in the oxidation of micropollutants: a mini review, Front. Environ. Sci. Eng. China 4 (4) (2010) 405–413, https://doi.org/10.1007/s11783-010-0252-8.
[10] J.-M. Herrmann, Heterogeneous photocatalysis: fundamentals and applications to the removal of various types of aqueous pollutants, Cataly. Today 53 (1) (1999) 115–129, https://doi.org/10.1016/S0920-5861(99)00107-8.
[11] M.I. Pariente, R. Molina, J.A. Melero, J.A. Botas, F. Martinez, Intensified-Fenton process for the treatment of phenol aqueous solutions, Water Sci. Technol. 71 (2015) 359–365, https://doi.org/10.2166/wst.2014.515.
[12] M. Kuosa, J. Kallas, A. Häkkinen, Ozonation of p-nitrophenol at different pH values of water and the influence of radicals at acidic conditions, J. Environ. Chem. Eng. 3 (1) (2015) 325–332.
[13] J. Sun, X. Meng, Y. Shi, R. Wang, S. Feng, D. Jiang, R. Xu, F.-S. Xiao, A novel catalyst of Cu–Bi–V–O complex in phenol hydroxylation with hydrogen peroxide, J. Catal. 193 (2) (2000) 199–206, https://doi.org/10.1006/jcat.2000.2901.
[14] C. Xiong, Q. Chen, W. Lu, H. Gao, W. Lu, Z. Gao, Novel Fe-based complex oxide catalysts for hydroxylation of phenol, Catal. Lett. 69 (2000) 231–236, https://doi.org/10.1023/A:1019042527870.
[15] L.F. Liotta, M. Gruttadauria, G. Di Carlo, G. Perrini, V. Librando, Heterogeneous catalytic degradation of phenolic substrates: catalysts activity, J. Hazard. Mater. 162 (2-3) (2009) 588–606, https://doi.org/10.1016/j.jhazmat.2008.05.115.
[16] M.R. Maurya, S.J.J. Titinchi, S. Chand, Oxidation of phenol with H2O2 catalysed by Cu (II), Ni (II) and Zn (II) complexes of N, N′-bis-(salicylidene) diethylenetriamine (H2saldien) encapsulated in Y-zeolite, J. Mol. Catal. A Chem. 201 (1-2) (2003) 119–130, https://doi.org/10.1016/S1381-1169(03)00193-6.
[17] X.-G. Meng, J. Zhu, J. Yan, J.-Q. Xie, X.-M. Kou, X.-F. Kuang, L.-F. Yu, X.-C. Zeng, Studies on the oxidation of phenols catalyzed by a copper (II)–Schiff base complex in aqueous solution under mild conditions, J. Chem. Technol. Biotechnol. 81 (1) (2006) 2–7, https://doi.org/10.1002/jctb.1349.
[18] E.A. Karakhanov, A.L. Maximov, Y.S. Kardasheva, V.A. Skorkin, S.V. Kardashev, E. A. Ivanova, E. Lurie-Luke, J.A. Seeley, S.L. Cron, Hydroxylation of phenol by hydrogen peroxide catalyzed by copper(II) and iron(III) complexes: the structure of the ligand and the selectivity of ortho-hydroxylation, Ind. Eng. Chem. Res. 49 (10) (2010) 4607–4613, https://doi.org/10.1021/ie902040m.
[19] E. Derouane, Shape selectivity in catalysis by zeolites - the nest effect, J. Catal. 100 (2) (1986) 541–544, https://doi.org/10.1016/0021-9517(86)90127-2.
[20] E.G. Derouane, J.M. Andre, A.A. Lucas, Surface curvature effects in physisorption and catalysis by microporous solids and molecular-sieves, J. Catal. 110 (1988) 58–73, https://doi.org/10.1016/0021-9517(88)90297-7.
[21] P.-J. Yu, C.-C. Hsieh, P.-Y. Chen, B.-J. Weng, Y.W. Chen-Yang, Highly active and reusable silica-aerogel-supported platinum–cobalt bimetallic catalysts for the dehydrogenation of ammonia borane, RSC Adv. 6 (113) (2016) 112109–112116, https://doi.org/10.1039/C6RA24249A.
[22] B.C. Dunn, P. Cole, D. Covington, M.C. Webster, R.J. Pugmire, R.D. Ernst, E. M. Eyring, N. Shah, G.P. Huffman, Silica aerogel supported catalysts for Fischer-Tropsch synthesis, Appl. Catal. A 278 (2) (2005) 233–238, https://doi.org/10.1016/j.apcata.2004.10.002.
[23] C.-T. Wang, S.-H. Ro, Nanocluster iron oxide-silica aerogel catalysts for methanol partial oxidation, Appl. Catal. A 285 (1-2) (2005) 196–204, https://doi.org/10.1016/j.apcata.2005.02.029.
[24] J. Choi, C.B. Shin, D.J. Suh, Co-promoted Pt catalysts supported on silica aerogel for preferential oxidation of CO, Catal. Commun. 9 (5) (2008) 880–885, https://doi.org/10.1016/j.catcom.2007.09.036.
[25] H.F. Bereczki, L. Daroczi, I. Fabian, I. Lazar, Sol-gel synthesis, characterization and catalytic activity of silica aerogels functionalized with copper(II) complexes of cyclen and cyclam, Micropor. Mesopor. Mat. 234 (2016) 392–400, https://doi.org/10.1016/j.micromeso.2016.07.026.
[26] I. Lázár, H.F. Bereczki, S. Manó, L. Daróczi, G. Deák, I. Fábián, Z. Csernátony, Synthesis and study of new functionalized silica aerogel poly(methyl methacrylate) composites for biomedical use, Polym. Compos. 36 (2) (2015) 348–358, https://doi.org/10.1002/pc.22949.
[27] I. Lazar, I. Fabian, A continuous extraction and pumpless supercritical CO2 drying system for laboratory-scale aerogel production, Gels 2 (2016) 26, https://doi.org/10.3390/gels2040026.
[28] L. Juhasz, K. Moldovan, P. Gurikov, F. Liebner, I. Fabian, J. Kalmar, C. Cserhati, False morphology of aerogels caused by gold coating for SEM imaging, Polymers 13 (2021) 588, https://doi.org/10.3390/polym13040588.
[29] G. Beaucage, Approximations leading to a unified exponential power-law approach to small-angle scattering, J. Appl. Crystallogr. 28 (1995) 717–728, https://doi.org/10.1107/S0021889895005292.
[30] S.M. King, Small-angle neutron scattering, Modern techniques for polymer characterisation, John Wiley & Sons Ltd., Chichester, 1999, pp. 171–232.
[31] A. Rockenbauer, L. Korecz, Automatic computer simulations of ESR spectra, Appl. Magn. Reson. 10 (1-3) (1996) 29–43, https://doi.org/10.1007/BF03163097.
[32] T. Ditrói, J. Kalmár, J.A. Pino-Chamorro, Z. Erdei, G. Lente, I. Fábián, Construction of a multipurpose photochemical reactor with on-line spectrophotometric detection, Photochem. Photobiol. Sci. 15 (4) (2016) 589–594.
[33] J. Qin, X. Tan, F. Feng, H.e. Li, Facile and controllable synthesis of AuCu aerogels for the enhanced degradation of 4-nitrophenol, Appl. Surf. Sci. 561 (2021) 150024, https://doi.org/10.1016/j.apsusc.2021.150024.
[34] A.K. Covington, R.G. Bates, R.A. Durst, Definition of Ph scales, standard reference values, measurement of Ph and related terminology - (recommendations 1984), Pure Appl. Chem., 57 (1985) 531-542. DOI: 10.1351/pac198557030531.
[35] S. Balamurugan, N. Naresh, I. Prakash, N. Satyanarayana, Capacity fading mechanism of Li2O loaded NiFe2O4/SiO2 aerogel anode for lithium-ion battery: Ex-situ XPS analysis, Appl. Surf. Sci. 535 (2021) 147677, https://doi.org/10.1016/j.apsusc.2020.147677.
[36] M. Thommes, K. Kaneko, A.V. Neimark, J.P. Olivier, F. Rodriguez-Reinoso, J. Rouquerol, K.S.W. Sing, Physisorption of gases, with special reference to the evaluation of surface area and pore size distribution (IUPAC Technical Report), Pure Appl. Chem. 87 (2015) 1051–1069, https://doi.org/10.1515/pac-2014-1117.
[37] C.J. Gommes, A.P. Roberts, Stochastic analysis of capillary condensation in disordered mesopores, Phys. Chem. Chem. Phys. 20 (19) (2018) 13646–13659.
[38] N.H. Borzęcka, B. Nowak, R. Pakuła, R. Przewodzki, J.M. Gac, Cellular automata modeling of silica aerogel condensation kinetics, Gels 7 (2021) 50, https://doi.org/10.3390/gels7020050.
[39] P. Veres, M. Kéri, I. Bányai, I. Lázár, I. Fábián, C. Domingo, J. Kalmár, Mechanism of drug release from silica-gelatin aerogel—Relationship between matrix structure and release kinetics, Colloids Surf. B 152 (2017) 229–237, https://doi.org/10.1016/j.colsurfb.2017.01.019.

[40] B. Hammouda, A new Guinier-Porod model, J. Appl. Crystallogr. 43 (4) (2010) 716–719, https://doi.org/10.1107/S0021889810015773.
[41] A. Otsuki, L. de Campo, C.J. Garvey, C. Rehm, H2O/D2O contrast variation for ultra-small-angle neutron scattering to minimize multiple scattering effects of colloidal particle suspensions, Coll. Interfac. 2 (2018) 37, https://doi.org/10.3390/colloids2030037.
[42] I. Lázár, A. Forgács, A. Horváth, G. Király, G. Nagy, A. Len, Z. Dudás, V. Papp, Z. Balogh, K. Moldován, L. Juhász, C. Cserháti, Z. Szántó, I. Fábián, J. Kalmár, Mechanism of hydration of biocompatible silica-casein aerogels probed by NMR and SANS reveal backbone rigidity, Appl. Surf. Sci. 531 (2020) 147232, https://doi.org/10.1016/j.apsusc.2020.147232.
[43] K. Miyoshi, H. Tanaka, E. Kimura, S. Tsuboyama, S. Murata, H. Shimizu, K. Ishizu, Electrochemical and spectroscopic studies on copper(Ii) complexes of macrocyclic ligands as models for square-pyramidal metal active-sites of copper(Ii) complexes of bleomycin and glutathione, Inorg. Chim. Acta 78 (1983) 23–30, https://doi.org/10.1016/S0020-1693(00)86483-X.
[44] M.C. Styka, R.C. Smierciak, E.L. Blinn, R.E. DeSimone, J.V. Passariello, Copper(II) complexes containing a 12-membered macrocyclic ligand, Inorg. Chem. 17 (1) (1978) 82–86, https://doi.org/10.1021/ic50179a018.
[45] H. Liu, J.Y. Zhu, X.S. Chai, In situ, rapid, and temporally resolved measurements of cellulase adsorption onto lignocellulosic substrates by UV-vis spectrophotometry, Langmuir 27 (1) (2011) 272–278, https://doi.org/10.1021/la103306v.
[46] Q.Q. Wang, J.Y. Zhu, C.G. Hunt, H.Y. Zhan, Kinetics of adsorption, desorption, and re-adsorption of a commercial endoglucanase in lignocellulosic suspensions, Biotechnol. Bioeng. 109 (8) (2012) 1965–1975, https://doi.org/10.1002/bit.24483.
[47] M.H. Robbins, R.S. Drago, Activation of hydrogen peroxide for oxidation by copper (II) complexes, J. Catal. 170 (2) (1997) 295–303, https://doi.org/10.1006/jcat.1997.1754.
[48] T. Lin, C. Wu, Activation of hydrogen peroxide in copper(II)/amino acid/H2O2 systems: effects of pH and copper speciation, J. Catal. 232 (1) (2005) 117–126, https://doi.org/10.1016/j.jcat.2005.01.038.
[49] J. Li, A.N. Pham, R. Dai, Z. Wang, T.D. Waite, Recent advances in Cu-Fenton systems for the treatment of industrial wastewaters: Role of Cu complexes and Cu composites, J. Hazard. Mater. 392 (2020) 122261, https://doi.org/10.1016/j.jhazmat.2020.122261.
[50] H. Sigel, C. Flierl, R. Griesser, Metal ions and hydrogen peroxide. XX. On the kinetics and mechanism of the decomposition of hydrogen peroxide, catalyzed by the Cu2+-2,2'-bipyridyl complex, J. Am. Chem. Soc. 91 (5) (1969) 1061–1064, https://doi.org/10.1021/ja01033a004.
[51] G. Lente, Common Pitfalls, in: Deterministic Kinetics in Chemistry and Systems Biology: The Dynamics of Complex Reaction Networks, Springer International Publishing, Cham, 2015, pp. 111-129.
[52] G. Peintler, I. Nagypal, I.R. Epstein, Systematic design of chemical oscillators. 60. Kinetics and mechanism of the reaction between chlorite ion and hypochlorous acid, J. Phys. Chem. 94 (7) (1990) 2954–2958, https://doi.org/10.1021/j100370a040.
[53] R. Valenzuela, D. Contreras, C. Oviedo, J. Freer, J. Rodríguez, Copper catechol-driven Fenton reactions and their potential role in wood degradation, Int. Biodeter. Biodegr. 61 (4) (2008) 345–350, https://doi.org/10.1016/j.ibiod.2007.10.006.
[54] J. Kalmár, M. Kéri, Z. Erdei, I. Bányai, I. Lázár, G. Lente, I. Fábián, The pore network and the adsorption characteristics of mesoporous silica aerogel: adsorption kinetics on a timescale of seconds, RSC Adv. 5 (130) (2015) 107237–107246, https://doi.org/10.1039/C5RA21353C.